ACE: Automated CTF Estimation

Satya P. Mallick [a,b,*] Bridget Carragher [b] Clinton S. Potter [b]

David J. Kriegman [c]

[a] *Department of Electrical and Computer Engineering,*

University of Caifornia, San Diego

[b] *National Resource for Automated Molecular Microscopy,*

Department of Cell Biology

The Scripps Research Institute, La Jolla.

[c] *Department of Computer Science and Engineering,*

University of Caifornia, San Diego

Abstract

In this paper we present a completely automated algorithm for estimating the parameters of the contrast transfer function (CTF) of a transmission electron microscope. The primary contribution of this paper is the determination of the astigmatism prior to the estimation of the CTF parameters. The CTF parameter estimation is then reduced to a 1D problem using elliptical averaging. We have also implemented an automated method to calculate lower and upper cutoff frequencies to eliminate regions of the power spectrum which perturb the estimation of the CTF parameters. The algorithm is comprised of three optimization subproblems, two of which are proven to be convex. Results of the CTF estimation method are presented for images of carbon support films as well as for images of single particles embedded in ice and suspended over holes in the support film. A MATLAB implementation of the algorithm, called ACE, is freely available.

Key words: Transmission electron microscope, Contrast Transfer Function, Parameter Estimation.

PACS: 68.37.Lp

1 Introduction

One of the most exciting challenges for biology today is in understanding the molecular machinery of the cell as a working, dynamic system. The technique of cryo electron microscopy (cryoEM) has a unique role to play in addressing this challenge as it can provide structural information on large macromolecular complexes in a variety of conformational and compositional states while preserved under close to physiological conditions. Traditionally the methods for cryoEM have been time consuming and labor intensive, involving data acquisition, analysis and averaging of thousands to hundreds of thousands of images of the individual macromolecular complexes. Thus, over the last few years there has been considerable interest and substantial efforts devoted to developing automated methods to improve the ease of use and throughput of cryoEM ([1,2,3,4,5]).

A critical step in the processing and analysis of cryoEM images involves the estimation of a variety of factors that modulate the image of the specimen and which must be corrected in order to reconstruct the true object. Principal among these is the contrast transfer function (CTF) of the microscope. The effect of the CTF is to introduce spatial frequency dependent oscillations into the Fourier space representation of the image. These effects can be readily observed using an image of an amorphous carbon film where the power spectrum of the image exhibits a series of concentric ripples called Thon rings [6] (see Fig. 1). The troughs in the trans-

* Corresponding author.
Email address: spmallick@graphics.ucsd.edu (Satya P. Mallick).

form represent frequency values where the CTF goes through zero and reverses phase. The precise location of the zeroes in the CTF is determined by the defocus and spherical aberration of the microscope (see review by Wade [7], for example) whereas the overall shape of the pattern is determined by the amount of axial astigmatism in the objective lens of the microscope. The ripples are circular when the astigmatism is zero and progressively change to elliptical, parabolic and hyperbolic patterns as the astigmatism is increased. Estimating the position of the zeroes in the CTF and correcting the consequent phase reversals in the image is essential in interpreting any image beyond a resolution corresponding to the first zero of the CTF.

A further modulation of the frequency of the Fourier components of the image arises as a result of a variety of factors (finite electron source size, energy spread of the beam, drift, etc.) whose combined effect is to reduce the signal at high resolution and thus limit the overall resolution of the images. These combined effects can be modeled using an envelope function. Finally, the image contains a noise component which is normally estimated as an additive linear component.

The theory of contrast transfer in the electron microscope [8,9] provides a parametric form for the CTF, the envelope function and the background noise. Our objective is thus to automatically recover these parameters, which can then be used to restore the images. Given the necessity of correcting the CTF when attempting to reconstruct structures to high resolutions, many solutions for estimating the parameters of the CTF have been proposed, and several of these have been automated to some degree. However, most of the proposed solutions for estimating the astigmatism in the image are somewhat ad-hoc and for the most part the astigmatism is simply assumed to be negligible. In our own method which we present in this paper we have been focused on providing a completely automated solution that is compatible with ongoing efforts to improve the overall automation and throughput of the

entire process of cryoEM structural analysis. In order to account for astigmatism we first estimate the elliptical shape of the CTF rings using edge detection methods and then use elliptical averaging to improve the signal to noise ratio for the final estimate of the CTF, the envelope function and the noise. The algorithm has been implemented as a MATLAB routine and is freely avaiable.

2 Related Work

In this section we discuss prior work on automated CTF estimation. Early works on Contrast Transfer Theory are attributed to Hanszen [10] and Thon [6]. CTF estimation was initially performed manually. Initial automated work on CTF estimation include work by Frank et al.[11] and Henderson et al.[12] who tried to estimate all parameters of the CTF in one pass by minimizing an error function based on the modulus of the Fourier Transform. The envelope function parameters were not included in the fitting process. The drawback of such approaches was that they did not take advantage of the rotational symmetry of the CTF in the absence of astigmatism. Hence, the signal which was used for CTF estimation was extremely weak, thus leading to unreliable estimates of the CTF parameters. Primarily because of the low signal to noise ratio, the estimation of the envelope function was not feasible. In the absence of the knowledge of the envelope function and the noise statistics, Wiener filtering would not optimally restore the image.

Zhou et al. [13] averaged the power spectrum along concentric circles about the origin (i.e rotational averaging). They estimated the background by interpolating the values between local minima. Zhu et al. [14] used a similar approach but assumed a Gaussian distribution for the background. Rotational averaging improved the signal to noise ratio and hence improved the estimates of the CTF parameters. The drawback of this approach was the assumption of no astigmatism.

Tani et al. [15] pointed out that the rotationally averaged 1D estimate of the power spectrum when re-sampled as a function of the square of the frequency (which they referred to as the "q^2 plot") is periodic, assuming that the value of the spherical aberration (C_s) is negligible. They filtered the Fourier transform of the "q^2 plot" to get rid of some of the noise. Astigmatism was calculated by dividing the image into small sectors and rotational averaging was done inside each of the sectors. In essence, the elliptical Thon rings were approximated by small circular arcs. As pointed out by Tani et al. [15], averaging should ideally be done on points in the power spectrum with the same CTF value. Our approach of elliptical averaging achieves this goal.

In the last few years some new approaches were introduced. Fernández et al. [16] used autoregressive (AR) modeling for estimating the power spectrum, while the background noise was modeled as an exponential of a polynomial of the frequency. Following the same line of work Valázquez-Muriel et al. [17] used autoregressive moving averages (ARMA) to model the power spectrum. This series of work was significant because for the first time, effort was put into the estimation of the power spectrum before estimating the CTF parameters. However, their method of parameter adjustment is essentially an exhaustive search for parameters and does not provide any formal guarantees of convergence. Hence the program needs to run several times to get to the actual solution. Secondly, while adjusting the defocus parameter, astigmatism was assumed to be absent. Under such an assumption, rotational averaging would give much better estimates of the defocus.

Sander et al. [18] used multivariate statistical analysis to group power spectra having similar CTF parameters and used class averages to get an estimate of the power spectrum. They used an iterative scheme to determine the parameters of the CTF. This iterative scheme is in essense an exhaustive search for parameters which mini-

mize the correlation between the theoretical and acutal CTF. The exhaustive search is performed over a user defi ned region in the parameter space. It becomes computationally intensive if the user, chooses a large region. On the other hand, it becomes inaccurate if the user chooses a small region. Even this exhaustive search does not guarantee convergence to the global correlation maxima because for each step only one parameter is being varied.

Mindell et al. [19] used a smoothed version of the 2D estimate of the power spectrum as an estimate of the background. They sought to maximize the cross-correlation between a theoretical CTF and the background subtracted 2D estimate of the power spectrum by doing a exhaustive search for the two defoci defi ning the CTF and the angle of astigmatism. Such exhaustive search approaches are computationally very intensive.

Huang et al. [20] reduced the problem of background and envelope estimation to a constrained optimization problem. They solved the constrained optimization problem using the simplex algorithm of linear programming. They obtained an estimate of the CTF by compensating the 1D profi le of the estimated power spectrum for the background and envelope functions. A lower and higher cutoff frequency to exclude some parts of the power spectrum were also defi ned . Astigmatism was calculated by dividing the image into small sectors (as many as 60) and rotationally averaging in each sector as described by Tani et al. [15]. The method proposed by Huang et al. [20] is both elegant and mathematically convincing and we have used the idea of constrained optimization in our own implementation.

3 Theory

In this section we briefly describe the image formation equation based on the contrast transfer theory [8,9,21]. Under the linear model of contrast transfer in an elec-

tron microscope the following assumptions are made

- The CTF (c) and the envelope function (e) are both spatially invariant.
- The noise (n) is independent and additive.

With the above assumptions the image formation equation can be written as

$$i(x, y) = c(x, y) \otimes e(x, y) \otimes f(x, y) + n(x, y) \tag{1}$$

where (x, y) are the spatial domain variables. i, c, e, and n represent the image, the CTF, the envelope function, and the noise in spatial domain respectively. f is the projection of the particle being imaged and is called the structure factor. $\otimes$ refers to the convolution operator.

Taking the Fourier transform on both sides of equation 1, we get the image formation equation in the frequency domain.

$$\mathcal{I}(s_x, s_y) = \mathcal{C}(s_x, s_y)\mathcal{E}(s_x, s_y)\mathcal{F}(s_x, s_y) + \mathcal{N}(s_x, s_y) \tag{2}$$

where (s_x, s_y) denote the frequency domain variables, while $\mathcal{I}$, $\mathcal{C}$, $\mathcal{E}$, $\mathcal{F}$ and $\mathcal{N}$ denote the image, the CTF, the envelope function, the structure factor and the noise in frequency domain respectively.

In polar coordinates, Equation 2 can be rewritten as :

$$\mathcal{I}(s, \theta) = \mathcal{C}(s, \theta)\mathcal{E}(s, \theta)\mathcal{F}(s, \theta) + \mathcal{N}(s, \theta) \tag{3}$$

where, $s = \sqrt{s_x^2 + s_y^2}$ and $\theta = \arctan(s_y/s_x)$.

In the weak phase approximation, the following parametric form for the CTF was proposed by Wade [7]

$$\mathcal{C}(s, \theta) = \sqrt{1 - C_a^2}\sin(\gamma(s, \theta)) + C_a \cos(\gamma(s, \theta)) \tag{4}$$

The phase γ is given by

$$\gamma(s,\theta) = 2\pi\left(\frac{-C_s\lambda^3 s^4}{4} + \frac{z(\theta)\lambda s^2}{2}\right) \tag{5}$$

where, λ is the wavelength of electrons in the microscope, C_s is the spherical aberration of the lens, and z is the defocus.

In the presence of astigmatism, the defocus is dependent on θ and is governed by the following equation proposed by Henderson et al.[12]

$$z(\theta) = \frac{z_2 + z_1}{2} + \frac{z_2 - z_1}{2}\sin(2(\theta - \phi)) \tag{6}$$

where, z_1 and z_2 are the minimum and maximum defoci respectively. ϕ is the angle made by the major axis of the elliptical Thon rings with the x-axis.

The envelope function is a result of several phenomena such as the coherence of the electron beam, the lens current instability, specimen drift etc. Models for the envelope function have been proposed to account for the above phenomena [13,22,23,24,25,26,27]. An approximation of the envelope function, called the "B-factor" parametric form [26,27] is given by

$$\mathcal{E}(s) = e^{k - Bs^2} \tag{7}$$

In recent published work [20], the"B-factor" parametric form was found to be inadequate in describing the envelope function. Our own experiments indicate that a few additional parameters, as well as the "B-factor", reasonably describe the envelope function. We model the envelope function using the following empirical form

$$\mathcal{E}(s) = e^{-(k_1 + k_2\sqrt{s} + k_3 s + k_4 s^2)} \tag{8}$$

One of the empirical parametric forms for the noise spectrum which encompasses a wide range of different physical effects, including incoherent scattering, fi lm noise

and scanner noise [28], is given by

$$\mathcal{N}^2(s) = e^{-(n_1+n_2\sqrt{s}+n_3 s+n_4 s^2)} \tag{9}$$

Our experiments show that the noise spectrum in a large number of test images fi t the above noise model very accurately even for images recorded using a CCD camera. Therefore, we chose to use the above noise model.

4 The Algorithm

As described above, there are 12 parameters which describe the power spectrum of an image taken using a TEM; the two defoci (z_1 and z_2), the amplitude contrast C_a, the astigmatism angle ϕ, the four parameters of the envelope function (k_1, k_2, k_3 and k_4) and the four parameters of the noise function (n_1, n_2, n_3 and n_4). Before we proceed to estimate these parameters we do a re-parameterization. If we have the knowledge of one of the defoci, say z_2 , we can estimate the other defocus, say z_1, based on the knowledge of the ratio r of the major and minor axes of the elliptical Thon rings. Hence, we can get rid of one parameter z_1 and introduce a new parameter r. The new set of parameters are r, ϕ, z_2, C_a,k_1, k_2, k_3, k_4 n_1, n_2, n_3 and n_4.

It is not practically feasible to set up this parameter estimation problem as a single step optimization because of the large number of parameters. However, we can estimate certain parameters without any knowledge of the others. We propose a sequential algorithm in which a few parameters are calculated at each step. The sequence of steps are as follows:

(1) Determination of astigmatism parameters (r, ϕ) and elliptical averaging : The benefi t of the new parameterization is that we can estimate the parameters r and ϕ without any knowledge of the other parameters. Based on the estimated

r and ϕ elliptical averaging of the power spectrum then averages all points at same CTF phase (γ).

(2) Determination of a lower cutoff frequency (s_l) : A lower cutoff frequency is calculated to remove a region of the power spectrum which is dominated by the structure factor.

(3) Determination of noise parameters (n_1,n_2, n_3 and n_4) : Having estimated r and ϕ, the noise parameters are estimated independent of all remaining parameters.

(4) Determination of upper cutoff frequency (s_u) : The upper cutoff frequency is determined based on the energy contained in the noise subtracted power spectrum.

(5) Determination of envelope parameters (k_1, k_2, k_3 and k_4) : The envelope function parameters can then be calculated independent of the defocus (z_2) and amplitude contrast (C_a).

(6) Determination of CTF parameters (z_1,z_2 and C_a) : Finally z_2 and C_a are calculated. Based on the values of z_2 and r, z_1 can be calculated.

Below we describe each of these steps in detail.

4.1 Determination of astigmatism parameters

Astigmatism is an imaging artifact caused by misalignment of the microscope, especially the apertures [29]. The presence of astigmatism can be seen in different ways. In the image it appears as the streaking in the graininess of the support fi lm. A hole in the support fi lm of an astigmatic image appears to have both light and dark fringes at its boundary. The effect is most easily observed in the power spectrum of the image where the Thon rings are distorted. Fig. 2 illustrates power spectra with increasing levels of astigmatism. In an image with little or no astigmatism, the Thon rings are circular. The shape of the Thon rings changes from circular to

elliptic to parabolic and finally to hyperbolic with increasing astigmatism.

From a purely mathematical standpoint, the rings (level sets of the power spectrum) can be any conic section depending on the values of defoci z_1 and z_2.

$z_1 = z_2$	$\Rightarrow$The conic is a circle. See Fig 2(a).
$\frac{z_1}{z_2} > 0$	$\Rightarrow$The conic is an ellipse. See Fig 2(b-d).
$z_1 = 0$ or $z_2 = 0$	$\Rightarrow$The conic is a parabola. See Fig. 2(e).
$\frac{z_1}{z_2} < 0$	$\Rightarrow$The conic is an hyperbola. See Fig. 2(f).

We present a method for calculating astigmatism when the Thon rings are elliptical. The images with parabolic or hyperbolic Thon rings are never used in practice and should be automatically rejected by the algorithm. Automatic rejection of such images is an important feature required for complete automation of CTF estimation.

In the absence of astigmatism, the Thon rings are circular. Hence, rotational averaging of the power spectrum can be done, so that points with the same CTF phase γ are averaged. Rotational averaging gives a 1D power spectrum which has a higher signal to noise ratio than the 2D estimate of the power spectrum. This in turn leads to better estimation of the noise, envelope and CTF parameters.

In the presence of astigmatism, the Thon rings are elliptical. If the parameters of the family of the concentric ellipses could be estimated, averaging along ellipses could improve signal to noise ratio. In previous approaches [13,14,15,20] elliptical averaging was approximated by dividing the power spectrum into several sectors, doing rotational averaging in the small sectors and estimating the defocus separately for each sector. This procedure amounts to approximating the elliptical ring with a number of circular arcs. If the number of sectors is chosen to be large, the

approximation should be good. However, the number of points which are averaged decreases and this leads to inferior estimates of defocus and other CTF parameters. On the other hand, if the sectors are large, much of the elliptical boundary is approximated using a single circular arc which leads to a bad approximation. This was the primary criticism of using a 1D power spectrum instead of doing parameter estimation on the 2D power spectrum. In our algorithm we estimate the parameters of the family of ellipses first and then take an average along the elliptical boundary to get a 1D power spectrum. In this algorithm, parameter estimation using a 1D power spectrum should be superior to its 2D counterpart due to increased signal to noise ratio.

The two parameters which define the family of elliptical Thon rings are

(1) r : The ratio of the major and minor axes of the Thon rings .

(2) ϕ : The angle which the major axis makes with the x-axis.

Our algorithm is motivated by the following observation. Near the origin, the Thon rings are most prominent and the spacing between them is large. Far from the origin, the Thon rings start fading away and the spacing between them decreases drastically. Higher frequency rings can be blurred out by convolving the power spectrum estimate with a 2D Gaussian filter of large width. The most prominent gradient in the power spectrum is between the points where the power spectrum falls from a very high value to it's first minimum. Edge detection with a high threshold value successfully recovers a single Thon ring. Edges are points that are local maxima of the magnitude of the gradient (above a given threshold) along the direction of the gradient. A higher value of threshold leads to lesser number of edge pixels. In practice, we use the Canny edge detector [30] to detect the edges with a suitable threshold. All edges very close to the center are removed because if the defocus is

very large, the first edge ring is very small and therefore not reliable for estimating r and ϕ. A typical result of the edge detection algorithm is shown in Fig. 3(a). The location of the edge is different from the location of the first dark ring which corresponds to a local minima of the power spectrum.

Following the edge detection we fit an ellipse to the detected edges. Any conic section can be represented by the following parametric form

$$ax^2 + bxy + cy^2 + dx + ey = 1 \tag{10}$$

The conic given by equations 10 is a hyperbola, parabola or an ellipse depending on the following conditions

$b^2 - 4ac > 0 \Rightarrow$ The conic is a hyperbola

$b^2 - 4ac = 0 \Rightarrow$ The conic is a parabola

$b^2 - 4ac < 0 \Rightarrow$ The conic is an ellipse or a circle

One of the advantages of using this general conic parameterization is that we can detect images with parabolic and hyperbolic Thon rings and reject them. Additionally, if the conic exhibits reflection symmetry about the origin (which means that if a point (x_1, y_1) satisfies equation 10, then point $(-x_1, -y_1)$ also satisfies Equation 10), then the equation of the conic reduces to

$$ax^2 + bxy + cy^2 = 1 \tag{11}$$

A simple translation of the detected edge coordinates shifts the center of the ellipse to the origin. Hence, we use equation 11 as the equation of our ellipse. Also note that equation 11 is linear in parameters a, b and c, and so it is natural to consider linear least squares estimation. However, a linear estimator which minimizes the

least square error might not be the appropriate choice for estimating the parameters because spurious edges (outliers) may be detected if the threshold of the Canny edge detector is not chosen properly. See Fig. 4(a). One approach would be to filter out these spurious edges based on connectivity and length of the edges. Our experiments showed that such an approach was not robust enough. To deal with outliers we use the robust estimation technique of Random Sample Consensus (RANSAC) [31].

RANSAC, unlike least squares estimate, is robust to outliers. See Fig. 4 for an illustration. A brief description of the RANSAC algorithm follows. Assume that the minimum number of data points needed to estimate a parameter vector $\overrightarrow{p}$ is N and there are M data points in all. RANSAC has the following steps:

(1) Randomly select N data points out of M data points.
(2) Estimate the parameter vector $\overrightarrow{p}$ using the N selected points. The estimation procedure for this step can be any non-robust method.
(3) Find how many data points (of M) fit the model with parameter vector $\overrightarrow{p}$ within a user defined tolerance. Call this K.
(4) If K is big enough, accept fit and exit with success.
(5) Repeat the above steps for a user defined number of times.
(6) Exit with failure.

For step 2 of RANSAC we use the linear least squares estimate. The astigmatic

parameters (r, ϕ) can be calculated from the ellipse parameters a, b and c by

$$l_1 = \frac{a+c}{2} - \frac{1}{2}\sqrt{(a-c)^2 + b^2}$$
$$l_2 = \frac{a+c}{2} + \frac{1}{2}\sqrt{(a-c)^2 + b^2}$$
$$\phi = \arctan\left(\frac{2(l_2 - a)}{b}\right) \tag{12}$$
$$r = \sqrt{\frac{l_1}{l_2}} \tag{13}$$

Consider a power spectrum with elliptical Thon rings parameterized by r and ϕ. All the points along an ellipse have the same CTF phase γ. Hence we can average all points along an ellipse to generate a 1D power spectrum. The elliptically averaged power spectrum is given by

$$\begin{aligned}\mathcal{I}^2(s) &= \int_0^{2\pi} \mathcal{I}^2(s_x(\theta), s_y(\theta))d\theta \\ &= \int_0^{2\pi} \mathcal{I}^2(rs\cos(\theta - \phi), s\sin(\theta - \phi))d\theta \end{aligned} \tag{14}$$

4.2 Determination of the lower cutoff frequency

At low frequency, the structure factor dominates the power spectrum. This region of the power spectrum adversely affects the estimation accuracy of the CTF parameters. To filter out the effects of the structure factor, a lower cuttoff frequency needs to be calculated. The power spectrum below this cutoff frequency is not used in the estimation of the CTF parameters.

As mentioned earlier, the edge ring corresponds to the region of maximum gradient in the power spectrum. The first dark Thon ring, contains this edge ring. The region inside the first edge ring is dominated by the structure factor. The location (frequency) of the local maxima of the 1D power spectrum which is closest to the edge

location is used as the lower cutoff frequency. Fig. 5 shows a 1D power spectrum. The first dotted line represents the lower cutoff frequency and we denote it by s_1.

4.3 Determination of the noise parameters

The estimate of the power spectrum is elliptically averaged to get a 1D power spectrum. Using the cutoff frequency calculated in the previous section, the 1D power spectrum corresponding to the lower frequency is removed. We denote this new 1D power spectrum by $\mathcal{P}(s)$. Hence, using equation 3, assuming that the data is uncorrelated with background noise and that elliptical averaging has been completed, we get

$$\mathcal{P}(s) = \mathcal{C}^2(s)\mathcal{E}^2(s)\mathcal{F}^2(s) + \mathcal{N}^2(s) \tag{15}$$

$\mathcal{P}(s)$ can be sampled at frequencies $\mathbf{s} = [s_1 s_2 .... s_T]^\top$. In the frequency range under consideration, if the frequency response due to structure is assumed to be white, then Equation 15 reduces to the following equation

$$\mathcal{P}(\mathbf{s}) = \mathcal{C}^2(\mathbf{s})\mathcal{E}^2(\mathbf{s}) + \mathcal{N}^2(\mathbf{s}) \tag{16}$$

Let $\hat{\mathcal{N}}^2(\mathbf{s})$ denote an estimate of $\mathcal{N}^2(\mathbf{s})$ and has a parametric form given by Equation 9. Under the assumption that the noise spectrum $\mathcal{N}^2(s)$ changes slowly as compared to the function $\mathcal{C}^2(s)$, the local minima of $\mathcal{P}(s)$ correspond to the zero crossings of the CTF. At a zero crossing of the CTF, the function $\mathcal{P}(s)$ has contribution from the noise spectrum only. To get an estimate of the noise spectrum $\mathcal{N}^2(\mathbf{s})$, we fit a curve$\hat{\mathcal{N}}^2(\mathbf{s})$ to $\mathcal{P}(\mathbf{s})$ such that $\hat{\mathcal{N}}^2(\mathbf{s})$ is strictly less than $\mathcal{P}(\mathbf{s})$.

Formally, to calculate $\hat{\mathcal{N}}^2(\mathbf{s})$ we minimize the objective function given by

$$O_N(n_1, n_2, n_3, n_4) = \| \log(\mathcal{P}(\mathbf{s})) - n_1 - n_2\sqrt{\mathbf{s}} - n_3\mathbf{s} - n_4\mathbf{s}^2\|^2 \tag{17}$$

under the constraints

$$\log(\mathcal{P}(\mathbf{s})) - n_1 - n_2\sqrt{\mathbf{s}} - n_3\mathbf{s} - n_4\mathbf{s}^2 \geq 0 \tag{18}$$

In vector notation we can restate the above problem as

$$\hat{\mathbf{n}} = \arg\min_{\mathbf{n}} \|\mathbf{An} - \mathbf{b}\|^2 \tag{19}$$

under the constraint

$$\mathbf{An} - \mathbf{b} \geq 0 \tag{20}$$

where,

$$\mathbf{A} = [\,\mathbf{1}_{T\times 1}\ \sqrt{\mathbf{s}}\ \mathbf{s}\ \mathbf{s}^2\,] \qquad \mathbf{b} = \log(\mathcal{P}(\mathbf{s})) \qquad \mathbf{n} = [\,n_1\ n_2\ n_3\ n_4\,]^\top$$

($\mathbf{1}_{T\times 1}$ is a column vector of length T with all elements 1).

This constrained least squares problem reduces to the form of quadratic programming given by

$$\hat{\mathbf{n}} = \arg\min_{\mathbf{n}}(\mathbf{n^T Bn} + \mathbf{c^T n}) \tag{21}$$

where $\mathbf{B} = \mathbf{A^T A}$ and $\mathbf{c} = -\mathbf{2A^T b}$ under the constraint

$$\mathbf{An} - \mathbf{b} \geq 0 \tag{22}$$

The convexity of a quadratic programming problem depends on whether or not the matrix $\mathbf{B}$ is positive semi defi nite. The matrix $\mathbf{B}$ is positive semi defi nite in the case of a constrained least squares problem, and so the quadratic programming problem is convex. Hence, it is guaranteed to converge to a global minima.

The constrained linear least squares problem is solved using an algorithm by Coleman and Li [32].

4.4 Determination of upper cutoff frequency

The upper cutoff frequency is determined based on the energy contained in the signal. The energy contained in the power spectrum after removing the contribution from the background noise and removing the region dominated by the structure factor is given by

$$E = \sum_{s=s_l}^{s_T} \left[\mathcal{I}^2(s) - \mathcal{N}^2(s)\right] \tag{23}$$

where, s_l is the lower cutoff frequency. We define an upper cutoff frequency (s_u), so that 95% of the energy E is contained between s_l and s_u. Formally,

$$\sum_{s=s_l}^{s_u} \left[\mathcal{I}^2(s) - \mathcal{N}^2(s)\right] = 0.95 \sum_{s=s_l}^{s_T} \left[\mathcal{I}^2(s) - \mathcal{N}^2(s)\right] \tag{24}$$

4.5 Determination of envelope function parameters

Several phenomena such as the coherence of the electron beam, the lens current instability and specimen drift lead to an exponential decrease in signal strength with frequency. The effects of all these phenomena are modeled using a single function called the envelope function. As discussed earlier, we use the following empirical form for the envelope function

$$\hat{\mathcal{E}}^2(\mathbf{s}) = e^{-(k_1 + k_2\sqrt{\mathbf{s}} + k_3\mathbf{s} + k_4\mathbf{s}^2)} \tag{25}$$

where, $\hat{\mathcal{E}}^2(\mathbf{s})$ represents an estimate of the envelope function. Let $\mathcal{M}(\mathbf{s}) = \mathcal{P}(\mathbf{s}) - \mathcal{N}^2(\mathbf{s})$ denote the background subtracted power spectrum. The same approach that was used to find parameters of $\hat{\mathcal{N}}^2(\mathbf{s})$ can be used to find the parameters of $\hat{\mathcal{E}}^2(\mathbf{s})$ with a minor modification. The curve $\hat{\mathcal{E}}^2(\mathbf{s})$ should be strictly greater than the function $\mathcal{M}(s)$. Hence, the objective function is given by

$$O_{\mathcal{E}}(k_1, k_2, k_3, k_4) = \| \log(\mathcal{M}(\mathbf{s})) - k_1 - k_2\sqrt{\mathbf{s}} - k_3\mathbf{s} - k_4\mathbf{s}^2 \|^2 \tag{26}$$

under the constraint

$$\log(\mathcal{M}(\mathbf{s})) - k_1 - k_2\sqrt{\mathbf{s}} - k_3\mathbf{s} - k_4\mathbf{s}^2 \leq 0 \tag{27}$$

The parameters k_1, k_2, k_3 and k_4 can be calculated in the same way as the parameters n_1, n_2, n_3 and n_4.

4.6 Determination of the CTF parameters

In this section we discuss the method used to calculate the parameters of the CTF namely the defocus z_2 and the amplitude contrast C_a. An estimate of the CTF is be given by

$$\hat{\mathcal{C}}^2(\mathbf{s}) = \frac{\mathcal{P}(\mathbf{s}) - \hat{\mathcal{N}}^2(\mathbf{s})}{\hat{\mathcal{E}}^2(\mathbf{s})} \tag{28}$$

A straight forward method would be to calculate the parameters using any constrained non-linear optimization method which minimizes the objective function

$$O_z = \|\hat{\mathcal{C}}^2(\mathbf{s}) - \mathcal{C}(\mathbf{s}, z_2, C_a)\|^2 \tag{29}$$

under the constraint

$$z_2 < 0 \text{ and } 0 \leq C_a \leq 0.2 \tag{30}$$

where, $\mathcal{C}(\mathbf{s}, z_2, C_a)$ is the theoretical CTF obtained by using the elliptically averaged version of Equation 4. This problem has enough local mimima to prevent any guarantee of convergence to the actual solution. However, if we provide the algorithm with an initial guess which is suffi ciently close to the solution, we can hope for convergence. A reasonable initial guess for the the amplitude contrast is 0. We use a simple but robust technique to calculate an initial estimate of the defocus as an initial estimate for the constrained non-linear optimization algorithm. $\hat{\mathcal{C}}^2(s)$ is smoothed using a moving average low pass fi lter and then the derivative is taken to fi nd local minima of$\hat{\mathcal{C}}^2(s)$. Let, m_1 ... m_r be the r local minima. In an ideal situation, m_i would correspond to the i^{th} zero crossing of the CTF. However, we need

to consider the possibility that some of the r minima could be spurious, and some of the actual minima could have been missed. We therefore define a set of defoci values z_{ij} given by

$$z_{ij} = \frac{2j + C_s\lambda^3 m_i^4}{2\lambda m_i^2} \tag{31}$$

where, z_{ij} is the defocus obtained by assuming that the i^{th} minimum corresponds to the j^{th} zero crossing of the CTF. Let, $\mathcal{C}(s, z_{ij})$ be the theoretical CTF obtained with the defocus values z_{ij} using equation 4. The initial value of defocus (say z_{init}) is obtained by

$$z_{init} = \arg\min_{z_{ij}} \|\hat{\mathcal{C}(s)}^2 - \mathcal{C}^2(s, z_{ij})\|^2 \tag{32}$$

The z_{init} so obtained is close to the true defocus. However for greater accuracy, we use this value as an initial condition for a constrained non-linear optimization algorithm [33] which minimizes the objective function given by equation 29 and under the constraint given by inequality 30.

5 Results

The algorithm described above was implemented in MATLAB, a high-level technical computing language and interactive environment for algorithm development, data visualization, data analysis, and numerical computation. The program is called ACE (Automated CTF Estimation) and requires the MATLAB image processing and optimization toolboxes. The user can choose to turn astigmatism estimation on or off. In the case when astigmatism estimation is turned off, circular rather than elliptical averaging is performed. First, as a proof of concept, we show detailed results for each step of the algorithm using carbon support films. We next show the accuracy of the algorithm on a set of images of carbon support films in which defocus has been systematically varied from 0.6μm under-focus to 6μm under-focus in steps of 0.2μm. This experiment was designed to prove the accuracy of the al-

gorithm up to a constant bias. Finally we show the practical utility of the algorithm by testing it on images of particles embedded in ice and suspended over holes in the carbon film.

5.1 Carbon support

The Thon rings are far more prominent in images of carbon support films than in images containing only protein specimens embedded in vitreous ice [7]. Thus, as a proof of concept, we first show detailed results of the performance of the algorithm on images of carbon support films. We start with a demonstration of the ellipse fitting algorithm. A typical result of the edge detection algorithm is shown in Fig. 3(a). To demonstrate the robustness of the algorithm toward outliers, we changed the parameters of the Canny edge detector to force spurious edges to be detected (Fig. 4(a)). A comparison of the least squares estimate and a RANSAC estimate, shown in Fig. 4(b) and (c), illustrates that whereas the least squares estimate is incorrect, RANSAC is able to reject the outliers to give the correct result. A typical result of the estimates of the lower and upper cutoff frequencies is shown in Fig. 5. All subsequent results are shown in the frequency region between the upper and lower cutoff frequency indicated by the dashed lines.

A typical result of the estimation of the lower and upper cutoff frequencies is shown in Fig. 5. All subsequent results are shown in the frequency region between the upper and lower cutoff frequency. A typical fit of noise spectrum $\hat{\mathcal{N}}^2(s)$ is shown in Fig. 6(a). Notice that the noise spectrum passes through the local minima and is strictly below the power spectrum. A typical fit of the square of the envelope function $\hat{\mathcal{E}}^2(s)$ is shown in Fig. 6(b). The square of the envelope function passes through the local maxima of the noise subtracted power spectrum and is strictly above it. Fig. 6(c) shows an estimate of the square of the CTF (CTF^2) found using

Equation 28. The CTF^2 corresponding to a crude estimate of the defocus value is shown in Fig. 7(a) using a dashed curve. The crude estimate is obtained from the local minima shown using red dots. Note that even with the crude estimate of defocus, many of the low frequency minima of the theoretical and estimated CTF^2 are aligned. This estimate is close to the real solution. This crude estimate is the initial value supplied to the non-linear constrained optimization algorithm to refine the estimate of defocus and amplitude contrast. The dashed curve in Fig. 7(b) shows the CTF^2 corresponding to refined estimates of defocus and amplitude contrast. Notice that with the refined estimate of defocus and amplitude contrast, the minima of the estimated and theoretical CTF^2 are aligned more closely, especially at higher frequencies. Finally we show a composite of the true power spectrum and the estimated power spectrum in Fig. 8 for a 2D visualization of the estimated CTF.

5.2 Defocus series experiment

We designed a defocus series experiment to test the accuracy of the algorithm. The defocus of the microscope was changed from 0.6 μm under-focus to 6 μm under-focus in steps of 0.2 μm without changing the astigmatism. Corresponding to each defocus setting an image of the carbon support film was recorded using a CCD camera. The motivation for designing such an experiment is as follows.

First, the accuracy with which defocus can be measured, depends to an extent on the value of defocus itself. For example, it is easier to estimate defocus in the far from focus images as compared to near to focus images. Hence, the accuracy of an algorithm should be tested on a wide range of defocus values.

Second, the microscope can set defocus increments very precisely, but the zero defocus, which is used as a reference to set defocus values, is difficult to set to a high

degree of accuracy. In other words, the zero defocus contains a zero error which introduces a bias in the defocus set by the microscope. Therefore, to test the accuracy of an algorithm, comparing the estimated defocus and the nominal defocus set by the microscope is not appropriate. However, the difference between two defocus values set by the microscope is independent of the zero error and is a suitable quantity to assume as ground truth for testing the effi ciency of the algorithm. Comparing the nominal and estimated change in defocus would prove the algorithm to be correct up to a constant bias.

With the above considerations in mind, a large (and practical) defocus range of 0.6 μm under-focus to 6 μm under-focus was chosen with small increments of 0.2 μm. The defocus was estimated for each image. The mean of the difference between successive defocus estimates was 0.2026 μm and the standard deviation was 0.0165 μm. The plot of the calculated defocus versus the nominal defocus is shown in Fig. 9. The solid line in Fig. 9 shows a straight line fi t through the data. The zero error, which is given by the y-axis offset, was found to be 0.085 μm. The entire experiment was fully automatic.

5.3 GroEL embedded in ice

The algorithm was next tested using images of single particles of GroEL embedded in vitreous ice and suspended over holes in the carbon support fi lm. A typical image is shown in Fig. 10. The 2D power spectrum of each image was obtained by cropping out overlapping regions of the image and averaging their power spectra. Fig. 11 shows the result of edge detection and ellipse fi tting for the image in Fig. 10 and the subsequent further stages of the algorithm are depicted in Fig. 12. The local minima in the CTF which are barely perceptible in Fig. 11, become much more prominent after the elliptical averaging step. Fig 12 (e) shows the theoretical

CTF^2 based on the initial estimate of defocus. The mean squared error between the theoretical CTF^2 (shown using dashed curve) and the estimate of CTF^2 (shown using solid curve) was calculated to be 0.0494. The mean squared error reduces to 0.0409 when the refined estimates of defocus and amplitude constrast are used for the calculation of the theoretical CTF^2 (Fig. 12 (f)). A visual comparison of Fig. 12 (e) and (f) also shows that the CTF^2 based on the refined estimate of defocus and amplitude contrast fits the estimate of the CTF^2 better.

The algorithm was applied to a total of 540 images of GroEL particles suspended over holes. With astigmatism turned off, the algorithm produced correct estimates (as verified by visual inspection of the fitted 1D power spectrum) of the CTF in 527 of the images (97.59% success rate). In 10 images (1.85%) the calculated parameters were incorrect and 3 images (0.56%) could not be processed at all. When the astigmatism estimation was turned on, 494 out of 540 images could be processed correctly (91.48% success rate). The success rate was reduced because the ellipse fitting algorithm failed as a result of there being more spurious edges than real ones. In 46 images (7.96 %), ACE calculated incorrect results while 3 images (0.56 %) could not be processed at all.

6 Discussion

We have implemented an automated algorithm for estimating the parameters of the CTF including the determination of astigmatism. The parameter estimation is very accurate when applying the algorithm to images of carbon support films. The problem becomes much more challenging when trying to estimate the CTF directly from images of protein specimens embedded in vitreous ice and suspended over holes in the carbon support film. One approach to this problem that has sometimes been taken is to estimate the defocus of the specimen using a nearby image of the

carbon support film. However, we can show that the assumption that the carbon support film and the specimen in the nearby hole are at the same defocus is not always valid. For example, in one particular experiment in which we measured both the defocus of the specimen over the hole as well as from the carbon support film outside of the hole we found that the differences can be as large as 0.5um. These results are shown in Fig. 13

The calculation of astigmatism is very robust for carbon images. However, when the two defoci are nearly the same (i.e. $r \approx 1$), the direction of the major axis is arbitrary. This is as expected because when $r \approx 1$, the Thon rings are circular. This does not affect the 1D averaging because no matter what direction of major axis is chosen, the value of $r \approx 1$ will result in circular averaging. For ice-embedded particle images, the accuracy of astigmatism estimation depends on the kind of particle being imaged. For small particles having a dense population in ice, like most of the GroEL images described in the Results section above, the estimation can be fairly reliable. However, for images with low densities of particles spurious edge detection results in a failure of the astigmatism estimation. For particles which exhibit strong internal symmetry, for example helical filaments like Tobacco Mosaic Virus (TMV), the ordered arrangement of the subunits results in a series of strong amplitudes in the power spectrum which interferes with the edge detection algorithm. For these situations, a possible approach is to use the carbon images near the location of the particles to estimate the astigmatism, as unlike defocus, this does not depend on the location of the imaged object. Once the astigmatism parameters have been estimated, the other parameters can be estimated directly from the particle images following elliptical averaging. This approach was used to estimate the CTF for 95 images of TMV embedded in ice with 100% success rate (as judged by visual inspection of the fitted CTF).

Without the ability to accurately estimate the astigmatism of acquired images, it is necessary to acquire images with the astigmatism set as close to zero as possible or to reject images exhibiting any noticeable astigmatism. However, if the parameters of astigmatism can be determined accurately, then Wiener filtering can in principle restore astigmatic images as accurately as non-astigmatic images. Various people have in the past raised the point that using astigmatic images for single particle reconstruction might be valuable in terms of avoiding resolution gaps resulting from the zeroes in the CTF. However as far as we are aware these discussions have not been published anywhere in the literature. This is perhaps an area for further investigation.

7 Conclusion

We have presented a completely automated method for the estimation of the CTF, the envelope function and the noise spectrum parameters of an image taken using a TEM. The method incorporates a novel way of estmating astigmatism, and reduces the problem of CTF estimation to a truly 1D estimation problem using elliptical averaging. The accuracy of the algorithm was demonstrated using images of carbon support film as well as on large datasets of single particles embedded in ice. A MATLAB implementation of the algorithm called ACE (Automated CTF Estimation) is freely available at:

`http://nramm.scripps.edu/software/ace`

8 Acknowledgements

Support for this work was provided by the National Resource for Automated Molecular Microscopy which is supported by the National Institutes of Health through the national Center for Research Resources (P41 program, grant RR17573). Additional

support for the project was provided by NIH (GM61939).

D. Kriegman was supportied in part under NSF Grants IIS-0308185 and NSF IIS 00-85980. S. Mallick was supported in part under NSF IIS 00-85980. Any opinions, fi ndings and conclusions or recommnedations expressed in this materials of those the authors, and do not necessarily reflect the views of the NSF.

References

[1] C. S. Potter, H. Chu, B. Frey, C. Green, N. Kisserberth, T. J. Madden, K. L. Miller, K. Nahrstedt, J. Pulokas, A. Reilein, et al., Leginon: A system for fully automated acquisition of 1000 micrographs a day, Ultramicroscopy 77 (1999) 153–161.

[2] B. Carragher, N. Kisserberth, D. Kriegman, R. A. Milligan, C. S. Potter, J. Pulokas, A. Reilein, LEGINON: An automated system for acquisition of images from vitreous ice specimens, Journal of Structural Biology 132 (2000) 33–45.

[3] Y. Zhu, B. Carragher, D. Kriegman, C. S. Potter, Automated identification of filaments in cryo-electron microscopy images, Journal of Structural Biology 135 (2001) 302–312.

[4] C. R. Booth, W. Jiang, W. Baker, Z. Hong Zhou, S. J. Ludtke, W. Chiu, A 9Å single particle reconstruction from ccd captured images on a 200kv electron cryomicroscope, Journal of Structural Biology 147 (2004) 116–127.

[5] P. Zhang, A. Beatty, J. L. S. Milne, S. Subramaniam, Automated data collection with tecnai 12 electron microscope: applications for molecular imaging by cryomicroscopy, Journal of Structural Biology 135 (2001) 251–261.

[6] F. Thon, Phase contrast electron microscopy, Electron Microscopy in Materials Science (1971) 570–625.

[7] R. H. Wade, A brief look at imaging and contrast transfer, Ultramicroscopy 46 (1992) 145–156.

[8] P. W. Hawkes, The electron microscope as a structure projector, Electron tomography (1992) 17–38.

[9] P. W. Hawkes, E. Kasper, Principles of electron optics: Wave Optics, Vol. 3, Academic Press, London, 1994.

[10] K. J. Hanszen, The optical transfer theory of the electron microscope: fundamental principles and applications, Advanced Optical and Electron Microscopy 4 (1971) 1–84.

[11] J. Frank, A study on heavy/light atom discrimination in bright field electron microscopy using the computer, Biophysical Journal 12 (1972) 484–511.

[12] R. Henderson, J. M. Baldwin, K. H. Downing, J. Lepault, F. Zemlim, Structure of purple membrane from halobacterium halobium: Recording, Mesurement and Evaluation of electron micrographs at 3.5 Åresolution, Ultramicroscopy 65 (1996) 31–44.

[13] Z. H. Zhou, W. Chiu, Prospects of using an IVEM with FEG for imaging macromolecules toward atomic resolution, Ultramicroscopy 49 (1993) 407–416.

[14] J. Zhu, J. Frank, Accurate retrieval of transfer function from defocus series, Proceedings of the 13th International Congress on Electron Microscopy 1 (1994) 465–466.

[15] K. Tani, H. Sasabe, C. Toyoshima, A set of computer programs for determining defocus and astigmatism in electron images, Ultramicroscopy 65 (1996) 31–44.

[16] J. A. Valázquez-Muriel, C. O. S. Sorzano, J. J. Fernández, J. Carazo, A method for estimating the CTF in electron microscopy based on ARMA models and parameter adjustment, Ultramicroscopy 96 (2003) 17–35.

[17] J. Fernández, J. Sanjurjo, J. Carazo, A spectral estimation approach to contrast transfer function detection in electron microscopy, Ultramicroscopy 68 (1997) 267–295.

[18] B. Sander, M. Golas, H. Stark, Automatic CTF correction for single particles based upon multivariate statistical analysis of individual power spectral, Journal of Structural Biology 142 (2003) 392–401.

[19] J. A. Mindell, N. Grigorieff, Accurate determination of local defocus and specimen tilt in electron microscopy., Journal of Structural Biology 142 (2003) 334–347.

[20] Z. Huang, P. R. Baldwin, S. Mullapudi, P. Penczek, Automated determination of parameters describing power spectra of micrograph images in electron microscopy, Journal of Structural Biology 144 (2003) 79–94.

[21] J. Frank, Three-dimensional electron microscopy of macromolecular assemblies, Academic Press, 1996.

[22] J. Frank, The envelope function of electron microscopic transfer function for partially coherent illumination, Optik 38 (1973) 519–536.

[23] R. H. Wade, J. Frank, Electron microscope transfer function for partially coherent axial illumination and chromatic defocus spread, Optik 49 (1977) 81–92.

[24] J. M. Kenney, J. Hantula, S. D. Fuller, L. Mindich, P. M. Ojala, D. H. Bamford, Bacteriophage phi 6 envelope elucidated by chemical cross-linking, immunodetection, and cryoelectron microscopy, Virology 190 (1992) 635–644.

[25] K. H. Downing, D. A. Grano, Analysis of photographic emulsions for electron microscopy of two-dimensional crystalline specimens, Ultramicroscopy 7 (1982) 381–404.

[26] J. Zhu, P. Penczek, R. Schröder, J. Frank, Three-dimensional reconstruction with contrast transfer function correction from energy-filtered cryoelectron micrographs: Procedure and application to the 70s *escherichia coli* ribosome, Journal of Structural Biology 118 (1997) 197–219.

[27] A. Saad, S. J. Ludtke, J. Jakana, F. J. Rixon, H. Tsuruta, W. Chiu, Fourier amplitude decay of electron cyromicroscopic images ofsingle particles and effects on structure determination, Journal of Structural Biology 133 (2001) 32–42.

[28] S. J. Ludtke, P. R. Baldwin, W. Chiu, EMAN: Semiautomated software for high resolution single-particle reconstructions, Journal of Structural Biology 128 (1997) 82–97.

[29] J. J. Bozolla, L. D. Russell, Electron Microscopy: Principles and Techniques for Biologists, 2nd Edition, Jones and Bartlett Publishers, 1992.

[30] J. Canny, A computational approach to edge detection, IEEE Transactions on Pattern Analysis and Machine Intelligence 8 (1986) 679–698.

[31] M. A. Fischler, R. C. Bolles, A paradigm for model fitting with applications to image analysis and automated cartography, Communications of the ACM 24 (1981) 381–395.

[32] T. F. Coleman, Y. Li, A reflective Newton method for minimizing a quadratic function subject to bounds on some of the variables, SIAM Journal on Optimization 6 (1996) 1040–1058.

[33] T. F. Coleman, Y. Li, An interior, trust region approach for non-linear minimization subject to bounds, SIAM Journal on Optimization 6 (1996) 418–445.

9 Figure captions

(1) Fig. 1: The power spectrum of an image of carbon support film. Concentric ripples called the Thon rings are due to the CTF.

(2) Fig. 2: Simulated power spectra with increasing astigmatism are shown. The caption shows the two defocus values corresponding to the power spectrum. The Thon rings can distort to an ellipse, a parabola or a hyperbola.

(3) Fig. 3: A typical result of edge detection and RANSAC estimation is shown. In (b) the two double headed arrows represent the estimated length and orientation of the major and minor axes.

(4) Fig. 4: In (a) result of a noisy edge detection is shown. In (b) and (c) the two double headed arrows represent the estimated length and orientation of the major and minor axes using least squares fit and RANSAC respectively. In (c) the additional blue points represent the inliers picked by RANSAC.

(5) Fig. 5: Determination of lower and upper cutoff frequencies and the fitting of noise spectrum and enevelope function. The solid blue curve represents the elliptically averaged 1D power spectrum. The lower cutoff frequency and the higher cutoff frequency are shown using dashed black vertical lines.The sum of noise spectrum and envelope function is shown by the green dashed curve. The noise spectrum is shown by a red dot-dash curve.

(6) Fig. 6: Estimation of the CTF^2. In (a) the solid curve shows the part of the power spectrum between the lower and upper cutoff frequency. The red dotted curve shows the estimated noise spectrum. In (b) the background subtracted 1D profile of the estimated power spectrum is shown using the solid curve. The estimated square of the envelope function is shown using the dashed green curve. In (c) an estimate of the CTF^2 is shown.

(7) Fig. 7: The result of defocus and amplitude contrast estimation is shown. The

blue curve is an estimate of the CTF^2 ($\hat{\mathcal{C}}^2(s)$). The red dashed curve in (a) is the theoretical CTF^2 obtained using the crude defocus estimate. The crude estimate of defocus is based on the local minima shown using red dots. In (b) defocus and amplitude contrast estimates are refi ned. Notice the local minima at higher frequencies are better aligned with the minima of the theoretical CTF^2 after refi nement.

(8) Fig. 8: A composite of the estimated (left) and observed power spectrum (right) in 2D is shown.

(9) Fig. 9: The plot of the calculated defocus versus the nominal defocus set by microscope is shown using dots. A line fi t to the above data points is also shown. The zero error, which can be seen in the y-axis offset, was found to be 0.085 μm.

(10) Fig. 10: The result shows a typical image of GroEL particles embedded in ice suspended in a hole. A section of the micrograph is zoomed in to show the density of the particles in the hole.

(11) Fig. 11: The result of edge detection and ellipse fi tting is shown.

(12) Fig. 12: (a) shows the elliptically averaged power spectrum. The vertical dashed lines in (a) show the estimated lower and upper cutoff frequency. In (b), the solid curve represents the part of the power spectrum between the lower and upper cutoff frequency. The dashed curve represents the estimate of noise spectrum ($\hat{\mathcal{N}}^2$). In (c) the solid curve represents the noise subtracted power spectrum and the dashed curve represents the estimate of the square of the envelope function ($\hat{\mathcal{E}}^2$). In (d) the estimate of the square of the CTF (CTF^2) recovered from the power spectrum is shown. In (e) the solid curve shows the estimated CTF^2 based on the power spectrum. The dashed curve shows the theoretical CTF^2 based on an initial estimate of defocus. The initial estimate

of the defocus was based on the local minima (shown using dots) of the estimated CTF^2 and was calculated using equation 32. The theoretical CTF^2 based on a refi ned estimate of defocus and amplitude contrast is shown in (f).

(13) Fig. 13: The plot of calculated defocus of the specimen in a hole versus defocus caluculated using carbon support fi lm outside of the hole is shown for a dataset containing 540 images(4096x4096) of GroEL embedded in ice. Notice that the defocus calculated using the images of carbon support fi lm can be very different from the actual defocus at the location of the specimen.

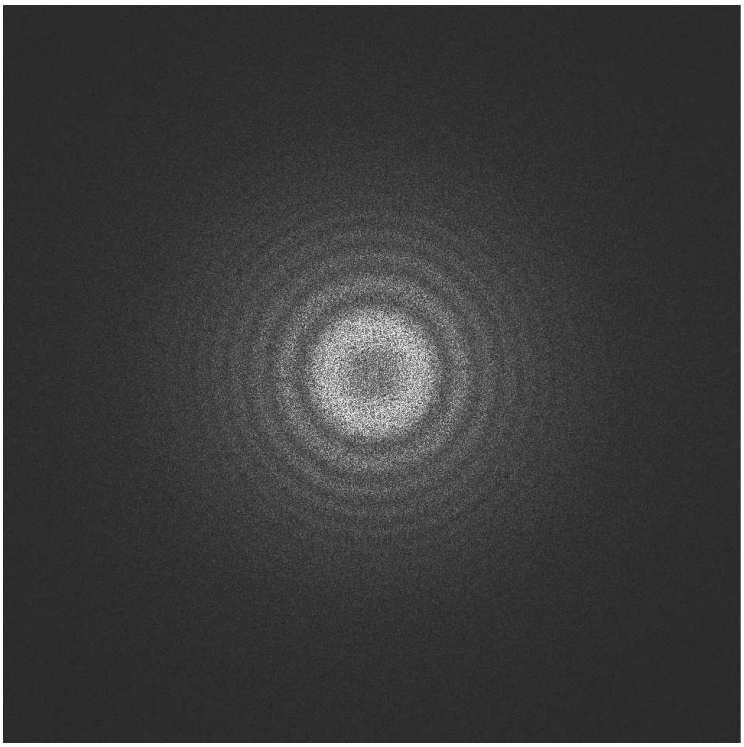

Fig. 1.

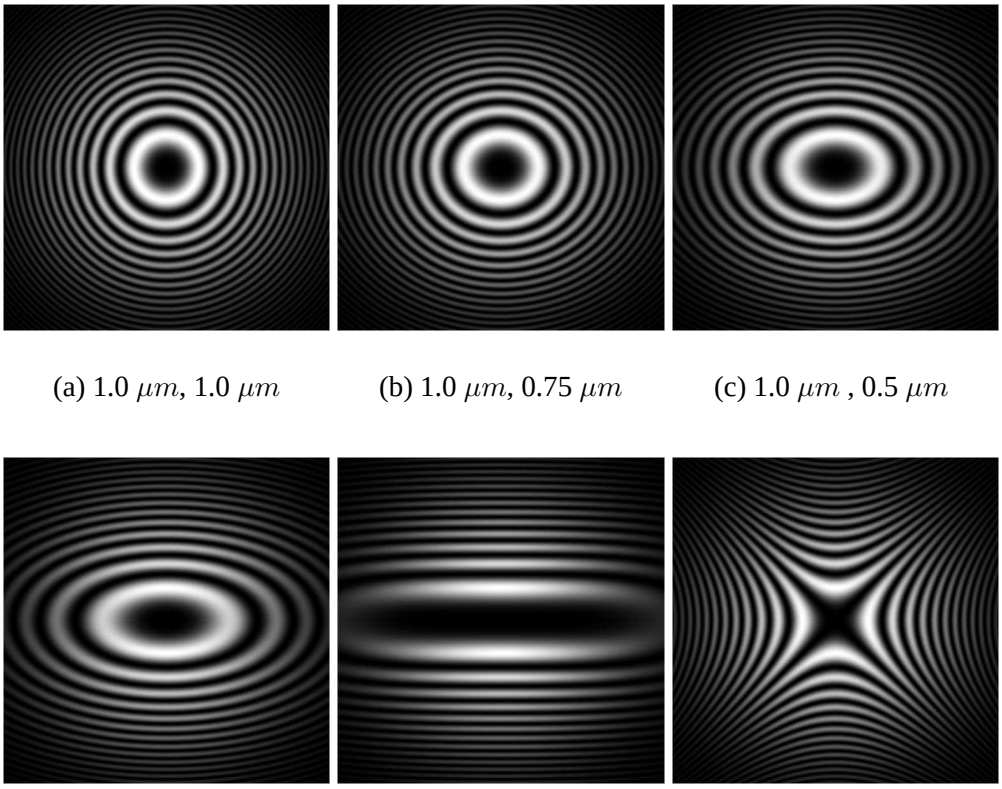

(a) 1.0 μm, 1.0 μm (b) 1.0 μm, 0.75 μm (c) 1.0 μm , 0.5 μm

(d) 1.0 μm, 0.25 μm (e) 1.0 μm, 0.0 μm (f) 1.0 μm, -1.0 μm

Fig. 2.

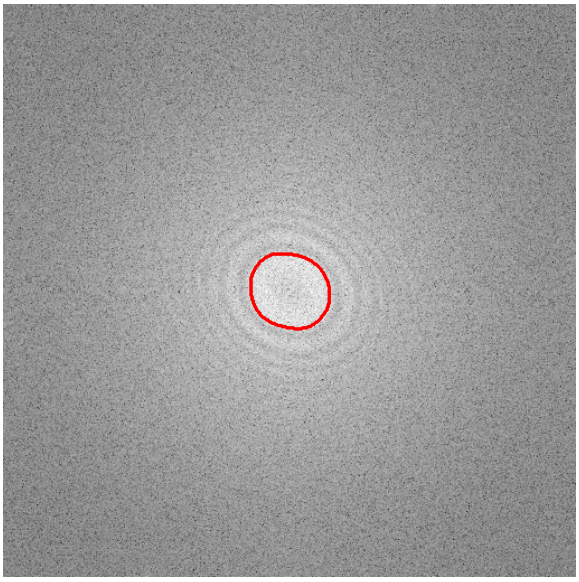

(a) Edge detection

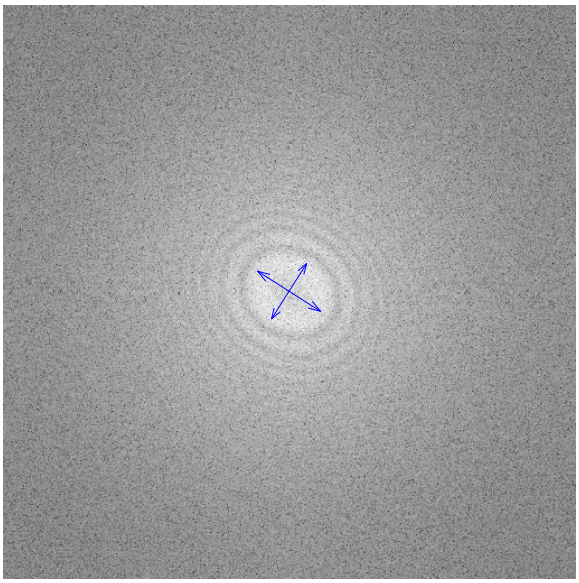

(b) RANSAC estimate

Fig. 3.

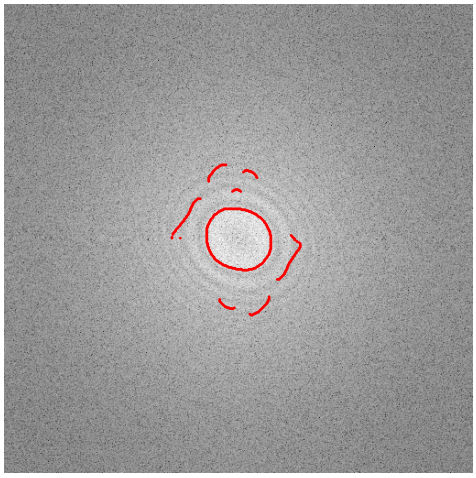

(a) Edge detection

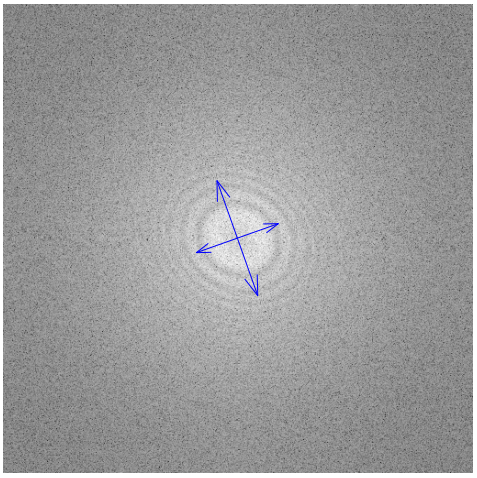

(b) LS estimate

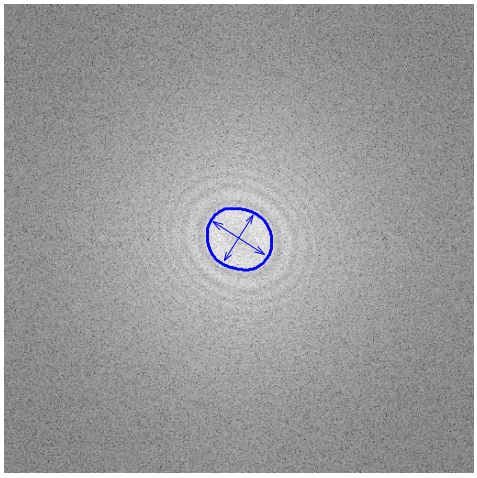

(c) RANSAC estimate

Fig. 4.

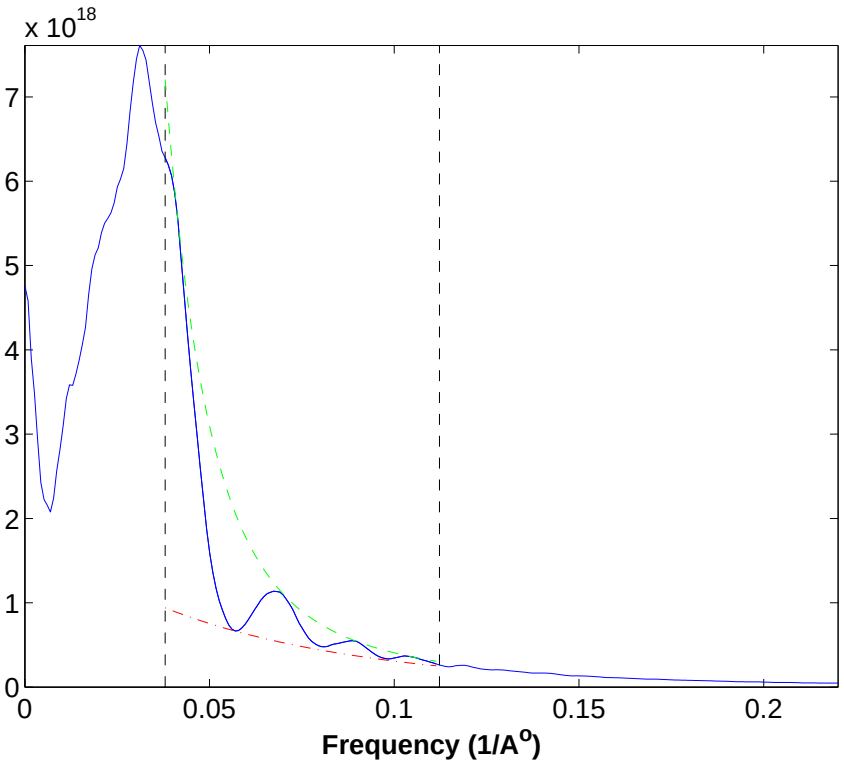

Fig. 5.

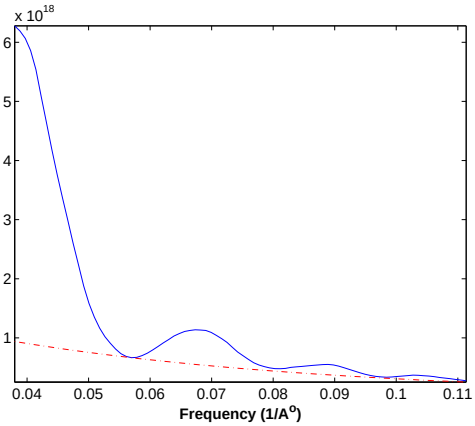

(a) $\hat{\mathcal{N}}^2(s)$

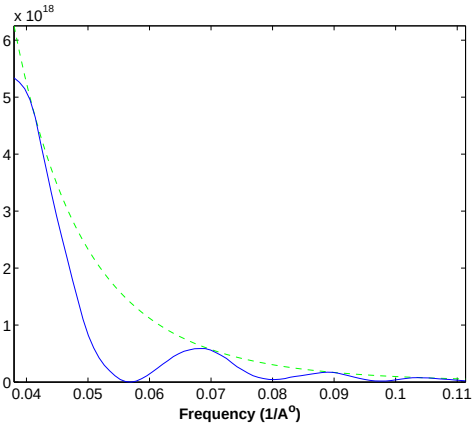

(b) $\hat{\mathcal{E}}^2(s)$

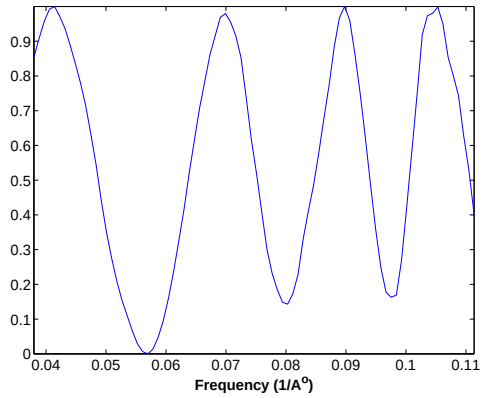

(c) $\hat{\mathcal{C}}^2(s)$

Fig. 6.

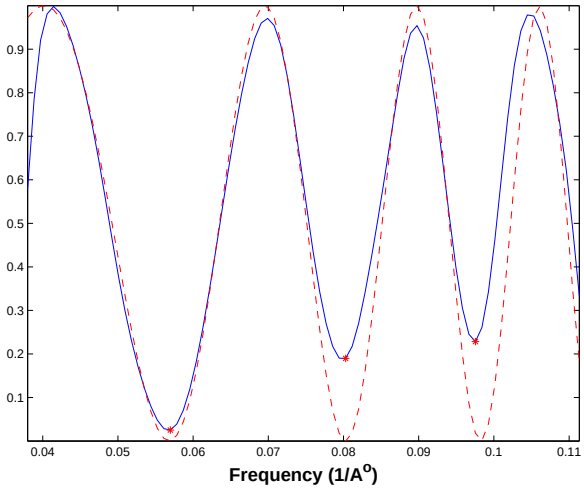

(a) Crude defocus estimate

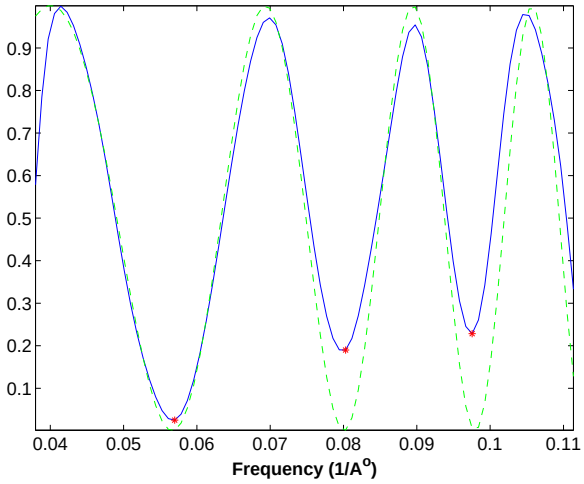

(b) Refined defocus estimate

Fig. 7.

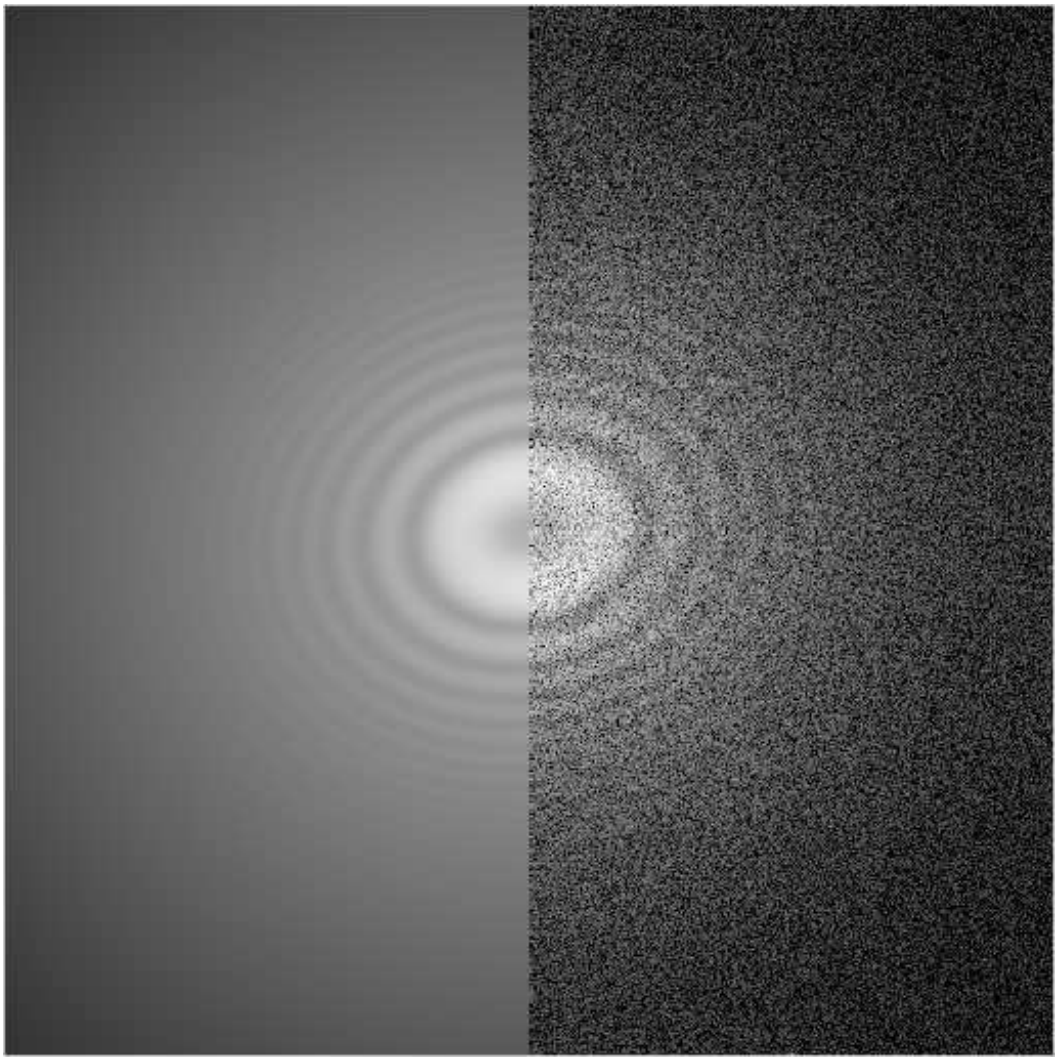

Fig. 8.

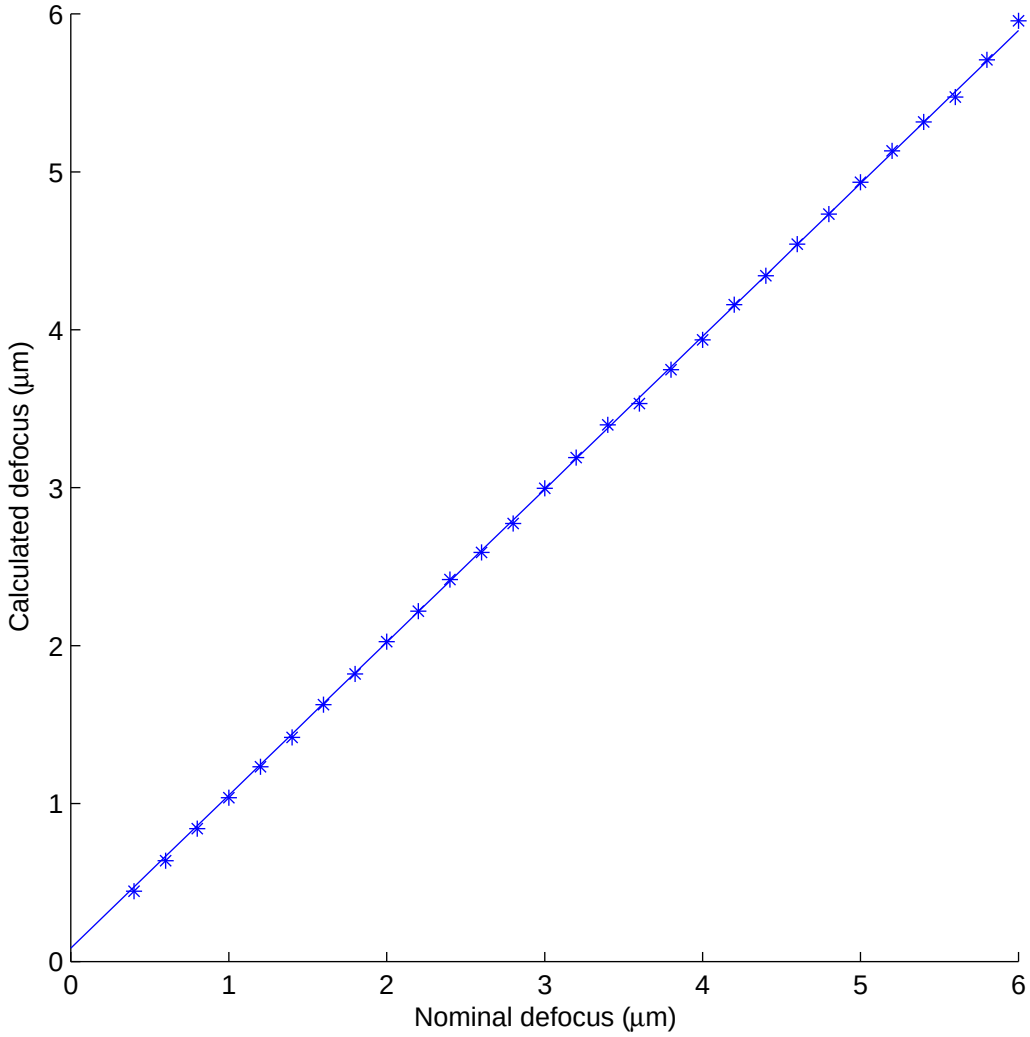

Fig. 9.

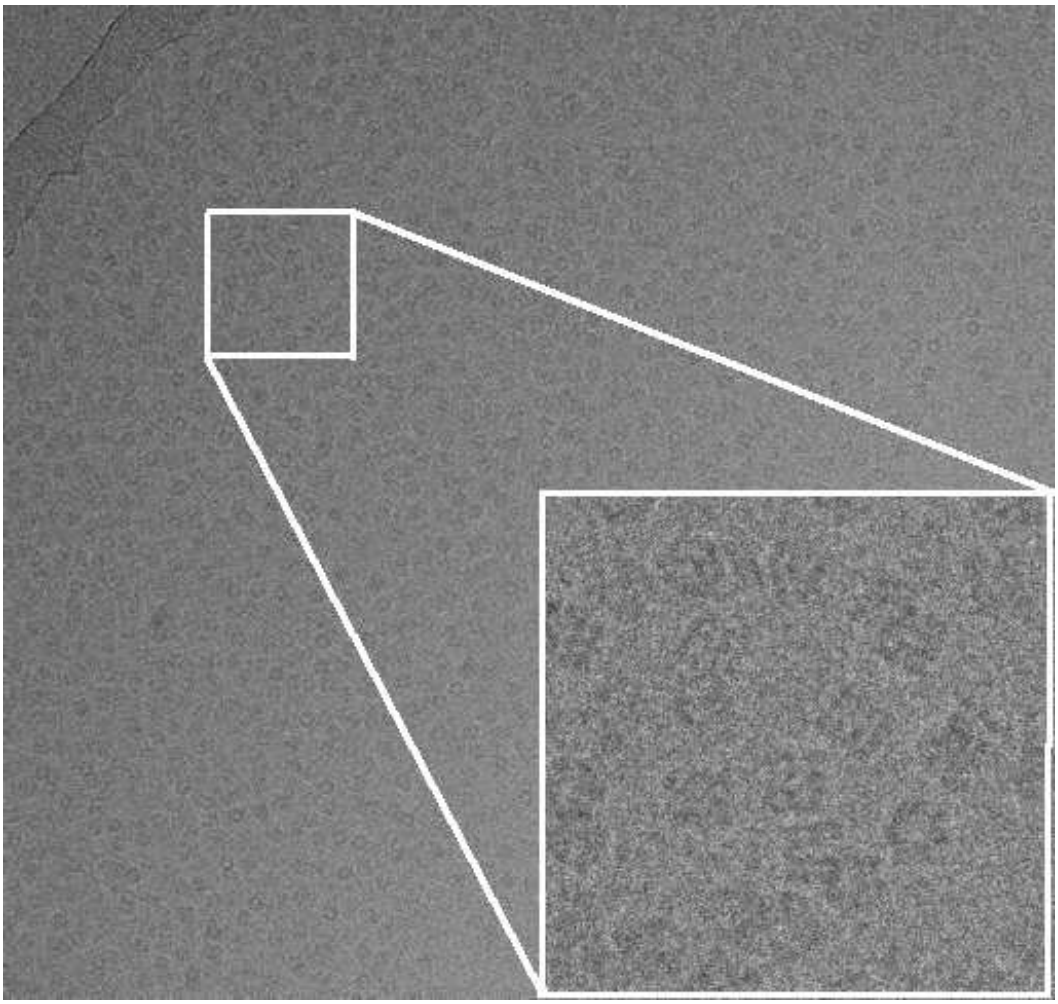

Fig. 10.

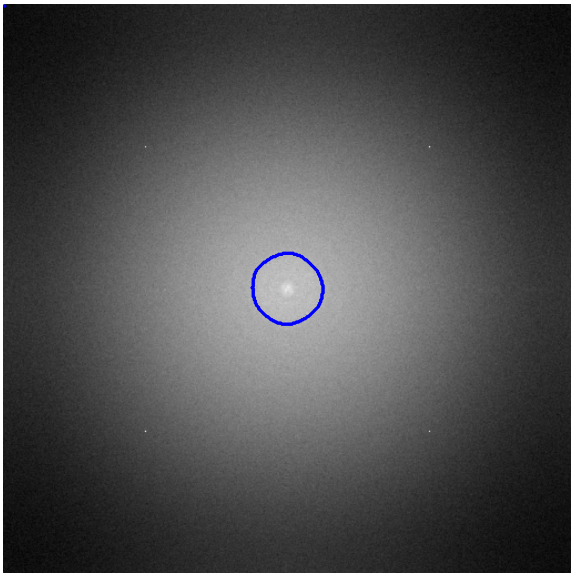

(a)

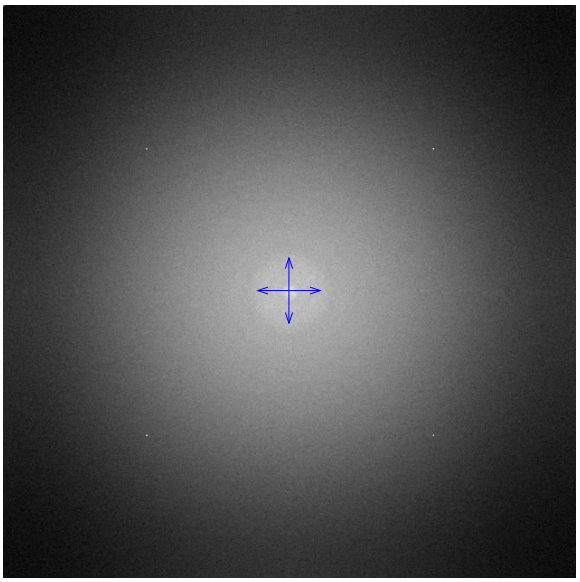

(b)

Fig. 11.

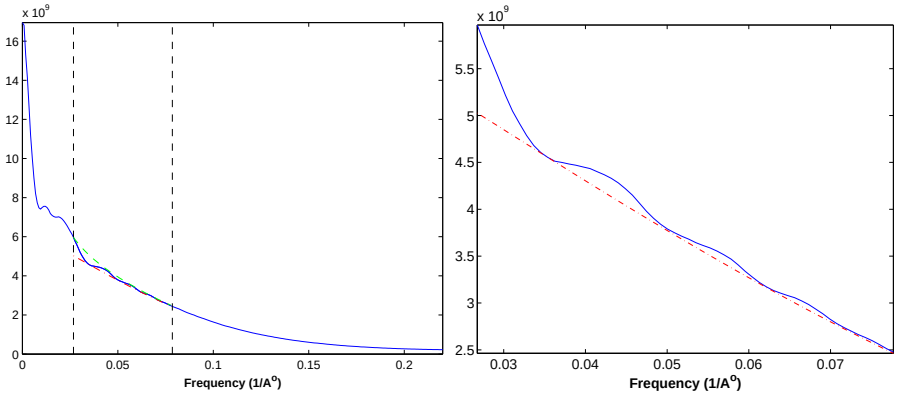

(a) s_l and s_u (b) $\hat{\mathcal{N}}^2(s)$

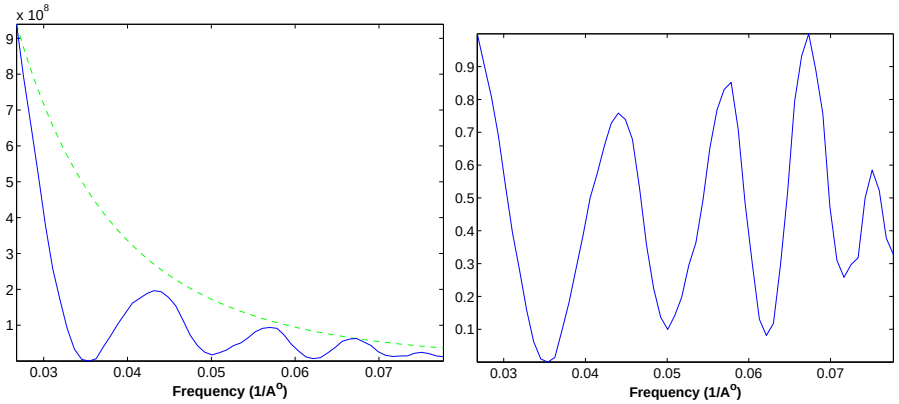

(c) $\hat{\mathcal{E}}^2(s)$ (d) $\hat{\mathcal{C}}^2(s)$

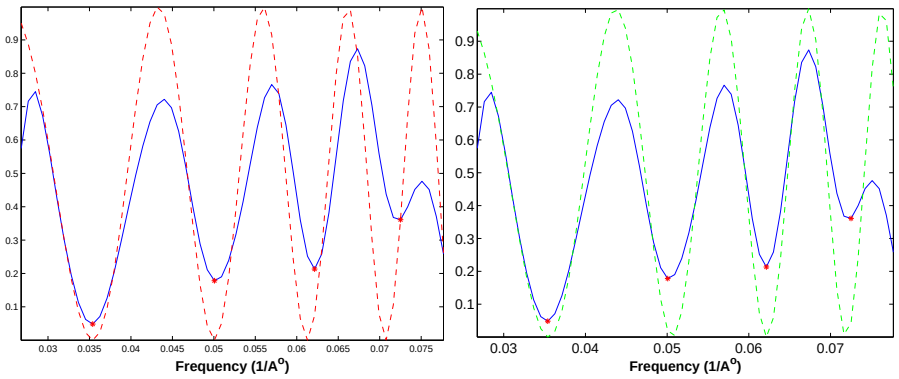

(e) Crude CTF estimate (f) Refined CTF estimate

Fig. 12.

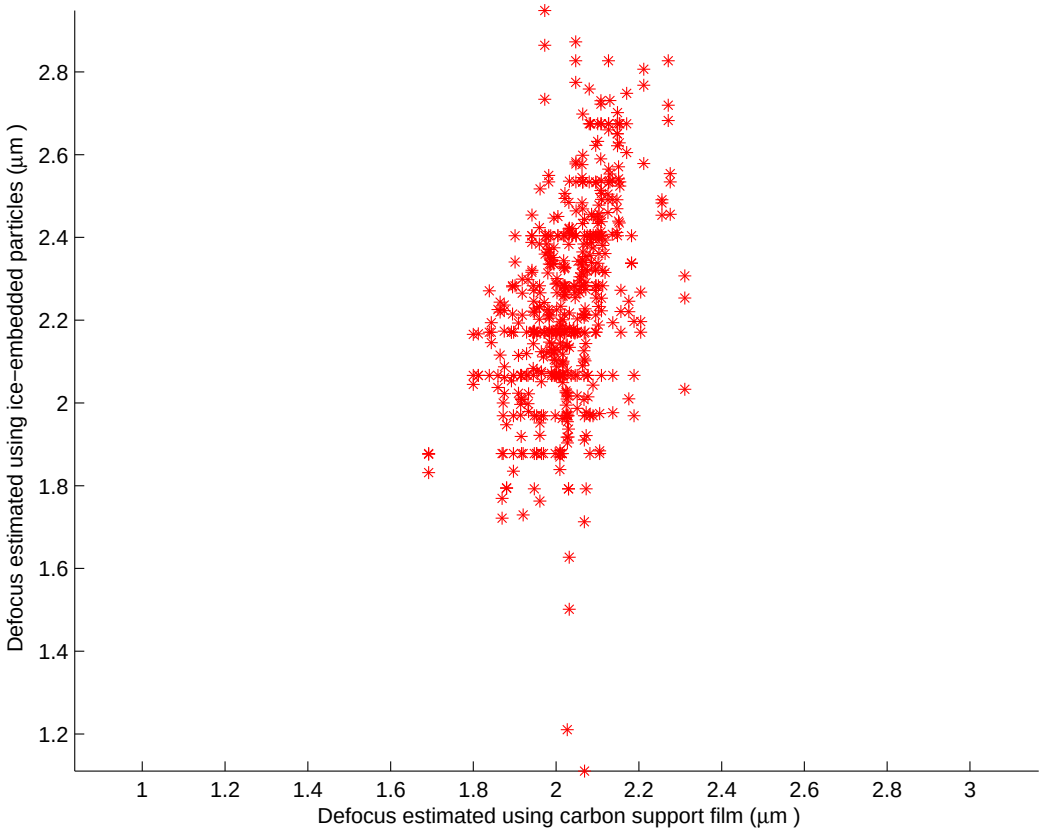
Defocus estimated using ice−embedded particles (µm)
Defocus estimated using carbon support film (µm)
2.8
2.6
2.4
2.2
2
1.8
1.6
1.4
1.2
1
1.2
1.4
1.6
1.8
2
2.2
2.4
2.6
2.8
3

Fig. 13.